# Tunneling magnetoresistance in magnetic tunnel junctions with a single ferromagnetic electrode

Kartik Samanta,[1,*,†] Yuan-Yuan Jiang,[2,3,*] Tula R. Paudel,[4] Ding-Fu Shao,[2,‡] and Evgeny Y. Tsymbal[1,§]

[1]*Department of Physics and Astronomy & Nebraska Center for Materials and Nanoscience, University of Nebraska, Lincoln, Nebraska 68588, USA*

[2]*Key Laboratory of Materials Physics, Institute of Solid-State Physics, HFIPS, Chinese Academy of Sciences, Hefei 230031, China*

[3]*University of Science and Technology of China, Hefei 230026, China*

[4]*Department of Physics, South Dakota School of Mines and Technology, Rapid City, South Dakota 57701, USA*

(Received 8 October 2023; accepted 12 April 2024; published 3 May 2024)

Magnetic tunnel junctions (MTJs) are key components of spintronic devices, such as magnetic random-access memories. Normally, MTJs consist of two ferromagnetic (FM) electrodes separated by an insulating barrier layer. Their key functional property is tunneling magnetoresistance (TMR), which is a change in MTJ's resistance when magnetization of the two electrodes alters from parallel to antiparallel. Here, we demonstrate that TMR can occur in MTJs with a single FM electrode, provided that the counterelectrode is an antiferromagnetic (AFM) metal that supports a spin-split band structure and/or a Néel spin current. Using $RuO_2$ as a representative example of such antiferromagnet and $CrO_2$ as a FM metal, we design all-rutile $RuO_2/TiO_2/CrO_2$ MTJs to reveal a nonvanishing TMR. Our first-principles calculations predict that magnetization reversal in $CrO_2$ significantly changes conductance of the MTJs stacked in the (110) or (001) planes. The predicted giant TMR effect of about 1000% in the (110)-oriented MTJs stems from spin-dependent conduction channels in $CrO_2$ (110) and $RuO_2$ (110), whose matching alters with $CrO_2$ magnetization orientation, while TMR in the (001)-oriented MTJs originates from the Néel spin currents and different effective $TiO_2$ barrier thickness for two magnetic sublattices that can be engineered by the alternating deposition of $TiO_2$ and $CrO_2$ monolayers. Our results demonstrate a possibility of a sizable TMR in MTJs with a single FM electrode and offer a practical test for using the antiferromagnet $RuO_2$ in functional spintronic devices.

DOI: 10.1103/PhysRevB.109.174407

## I. INTRODUCTION

Spintronics utilizes a spin degree of freedom in electronic devices to encode information [1]. A typical and widely used spintronic device is a magnetic tunnel junction (MTJ), which is composed of two ferromagnetic (FM) metal electrodes separated by a nonmagnetic insulating tunnel barrier [2–6]. The key functional property of an MTJ is tunneling magnetoresistance (TMR), which is a change of MTJ's resistance in response to magnetization reversal of the two FM electrodes from parallel to antiparallel [7]. The TMR effect can be as high as a few hundred percent [5,6], allowing the use of MTJs as building blocks of magnetic random-access memories [8].

The physics of TMR has been well understood in terms of spin-dependent tunneling that is controlled by the spin-polarized electronic band structure of ferromagnets and evanescent states of the tunneling barrier. In a crystalline MTJ, where the transverse wave vector is conserved in the tunneling process, wave functions belong to the symmetry group of the wave vector of the whole MTJ. This entails symmetry matching of the incoming and outcoming Bloch states in the electrodes and evanescent states in the barrier [9]. In particular, matching of the majority-spin $\Delta_1$ band in the Fe (001) electrode to the $\Delta_1$ evanescent state in the MgO (001) barrier layer is responsible for a large positive spin polarization and giant values of TMR predicted for crystalline Fe/MgO/Fe (001) MTJs [10]. Also, the complex band structure explains a large *negative* spin polarization of electrons tunneling from FM body-centered-cubic Co (001) through $SrTiO_3$ (001) tunneling barrier [11] consistent with the experimental observations [12,13]. It is now commonly accepted that the transport spin polarization of MTJs is controlled by the ferromagnet–barrier pair rather than the ferromagnet alone, which can be understood in terms of the interface transmission function [14].

In a two-terminal device, such as an MTJ, the spin polarization of the tunneling current cannot be detected on its own but requires a *magnetic* counterelectrode to measure TMR. This is because in a tunnel junction with a *nonmagnetic* counterelectrode, time-reversal operation $T$ flips the FM magnetization and reverses the current direction without changing the conductance magnitude, even in the presence of spin-orbit coupling [15]. While ferromagnets are commonly used as counterelectrodes in MTJs, the question arises if an antiferromagnet could be used instead to detect the tunneling spin polarization generated by a ferromagnet–barrier pair. This question is interesting not only from the fundamental point of view but also from the practical perspective, since in conventional MTJs, magnetization pinning of the counter FM electrode (a pinned layer) is often required, which is typically

*These authors contributed equally to this work.
†ksamanta2@unl.edu
‡dfshao@issp.ac.cn
§tsymbal@unl.edu

 

achieved using an exchange bias provided by an additional antiferromagnet (a pinning layer). Using an antiferromagnetic (AFM) counterelectrode instead would not require a pinning layer, simplifying the MTJ structure.

In this paper, we propose two approaches to realize an MTJ with a single FM electrode. The first approach exploits a low-symmetry oriented AFM counterelectrode that exhibits a spin-split band structure and uncompensated momentum-dependent spin polarization [16]. The second approach employs an AFM metal with strong intrasublattice coupling, revealing a staggered Néel spin current. To demonstrate these approaches, we consider $RuO_2$, a high Néel-temperature AFM metal, as a counterelectrode in all-rutile MTJs with an $CrO_2$ FM electrode and $TiO_2$ tunneling barrier. This choice of an AFM electrode is due to $RuO_2$ supporting a spin-polarized current in the [110] direction and a staggered Néel spin current in the [001] direction [17]. Using first-principles quantum-transport calculations [18–35], we predict sizable TMR for $RuO_2/TiO_2/CrO_2$ (110) and (001) MTJs.

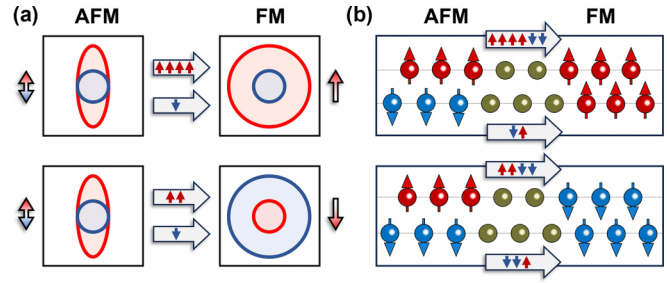


FIG. 1. Schematics of TMR in MTJs with a single FM electrode and an AFM counterelectrode. (a) TMR due to the anisotropic Fermi surface along a low-symmetry transport direction in an AFM electrode representing $RuO_2$ (110). Arrows indicate FM magnetization and double arrows indicate the Néel vector of the AFM layer. Red and blue curves represent up- and down-spin Fermi surfaces, respectively. (b) TMR due to the Néel spin current on two magnetic sublattices along a high-symmetry direction of the AFM electrode, representing $RuO_2$ (001).

## II. RESULTS

In crystalline MTJs, TMR is determined by the momentum-dependent spin polarization $p_\parallel(\vec{k}_\parallel)$ of the two electrodes, where $\vec{k}_\parallel$ is the wave vector transverse to the transport direction. A FM electrode hosts unbalanced $p_\parallel(\vec{k}_\parallel)$ resulting in a finite net-spin polarization. To employ an AFM metal as a counterelectrode in an MTJ, this antiferromagnet should also have unbalanced $p_\parallel(\vec{k}_\parallel)$ along the transport direction; otherwise, magnetization reversal would just flip spin contributions to MTJ's conductance without changing their magnitudes. Most compensated antiferromagnets, however, exhibit $\hat{P}\hat{T}$ and/or $\hat{T}\hat{t}$ symmetries, where $\hat{P}$ is space inversion, $\hat{T}$ is time reversal, and $\hat{t}$ is half a unit-cell translation, which enforce a spin-degenerate band structure and hence vanishing $p_\parallel(\vec{k}_\parallel)$. Thus, the desired AFM electrode must belong to a magnetic space group which does not have $\hat{P}\hat{T}$ and $\hat{T}\hat{t}$ among their symmetry operations. Among such antiferromagnets are certain types of collinear antiferromagnets [36–41], dubbed altermagnets [42–44], and noncollinear antiferromagnets [45,46]. These nonrelativistically spin-split antiferromagnets have been proposed for and utilized in AFM tunnel junctions (AFMTJs) [40,45–53]. Such AFM metals allow for nonzero net-spin polarization like ferromagnets [54]. This behavior is illustrated in Fig. 1(a), showing a spin-dependent Fermi surface of an antiferromagnet providing an unbalanced $p_\parallel(\vec{k}_\parallel)$ along the transport direction and hence a globally spin-polarized current resulting in a nonzero TMR in an MTJ with a single FM electrode.

Another strategy is to use a spin-degenerate antiferromagnet or a spin-split antiferromagnet with high-symmetry layer stacking that supports a Néel spin current (i.e., a staggered spin current on the two magnetic sublattices) [17]. In this case, certain kinds of *engineered* high-quality epitaxial MTJs may provide conditions for a nonzero TMR in a single-FM MTJ. Specifically, in MTJs where epitaxial layer-by-layer growth occurs through an alternating deposition of atoms to an atomic chain connecting each AFM sublattice to the FM electrode lattice, the effective barrier thickness for the two magnetic sublattices can be made unequal. This property is schematically depicted in Fig. 1(b), where two AFM sublattices carry Néel spin currents propagating across the barrier into a FM metal. Due to different effective barrier thickness for the two magnetic sublattices with electric currents flowing in parallel, TMR is nonzero.

The recently discovered AFM metal $RuO_2$ [55,56] supports a spin-polarized current along the [110] direction [40] and a Néel spin current along the [001] direction [17], and hence can serve as a counterelectrode in an MTJ with a single FM electrode. $RuO_2$ has a rutile structure with two AFM sublattices $Ru_A$ and $Ru_B$ [Fig. 2(a)]. The Néel vector is pointing along the [001] direction, and the Néel temperature is reported to be well above 300 K [55]. The required properties of $RuO_2$ originate from its magnetic space group $P4'_2/mnm'$ that has broken $\hat{P}\hat{T}$ and $\hat{T}\hat{t}$ symmetries, supporting spin splitting of the band structure. Specifically, the energy bands of bulk $RuO_2$ have a pronounced spin splitting along the high-symmetry $\Gamma$-$M$ and $Z$-$A$ lines, whereas they are spin degenerate along the $\Gamma$-$X$, $\Gamma$-$Z$, $X$-$M$, $Z$-$R$, and $R$-$A$ lines (Fig. S1(d) [18]). This fact indicates spin-polarized transport along the [110] direction and nonspin-polarized transport along the [001] direction in bulk $RuO_2$.

As a FM electrode, we consider $CrO_2$ that has a rutile structure [Fig. 2(b)] and belongs to space group $P4_2/mnm$ [57]. $CrO_2$ is a FM metal with the Curie temperature of 385–400K [58]. The majority-spin bands of bulk $CrO_2$ cross the Fermi energy while the minority-spin bands have a band gap that signifies half metallicity of $CrO_2$ (Fig. S1(d) [18]) and results in integer magnetization of 2 $\mu_B$/f.u. in the ground state [59,60]. We note here that the half-metallic nature of $CrO_2$ is not essential for TMR predicted in this paper.

The rutile space group $P4_2/mnm$ has fourfold rotational symmetry $C_4$ with respect to the [001] axis. While this symmetry is preserved by magnetism in $CrO_2$, it is broken in $RuO_2$. This is reflected in the Fermi surfaces of bulk $RuO_2$ and $CrO_2$. The Fermi surface of $RuO_2$ is spin split such that the up- and down-spin Fermi surfaces can be transformed to

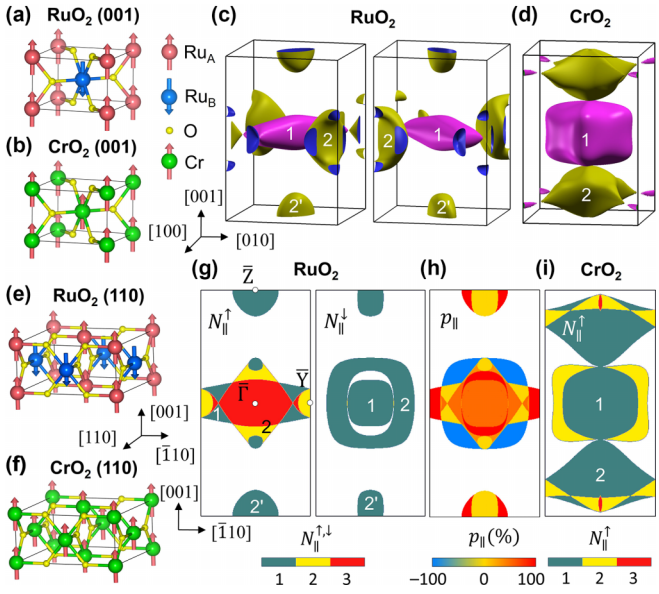


FIG. 2. (a), (b) Atomic and magnetic structure of $RuO_2$ (001) (a) and $CrO_2$ (001) (b). (c), (d) Fermi surfaces for up spin (left) and down spin (right) of $RuO_2$ (c) and for up spin of $CrO_2$ (d) with essential bands numbered. (e), (f) Supercells of $RuO_2$ (110) (e) and $CrO_2$ (110) (f). (g) Distribution of conduction channels in the 2DBZ for up spin (left) and down spin (right) of $RuO_2$ (110). High-symmetry points in the 2DBZ are indicated and essential contributing bands numbered. (h) Spin polarization of conduction channels in $RuO_2$ (110). (i) Same as (g) for up spin of $CrO_2$ (110).

each other by a 90° rotation around the [001] axis [Fig. 2(c)]. In contrast, the up-spin Fermi surface of $CrO_2$ has fourfold rotational symmetry with respect to the [001] axis [Fig. 2(d)]. Note that the down-spin Fermi surface does not exist due to half metallicity of $CrO_2$. As a result of these bulk symmetries, combining $RuO_2$ (001) and $CrO_2$ (001) as electrodes in an MTJ stacked in the (001) plane is not expected to produce TMR. On the contrary, transport along the {110} direction is expected to be spin polarized, resulting in a nonzero TMR effect.

The latter facts are evident from the number of conduction channels of bulk $RuO_2$ and $CrO_2$ along the transport direction, i.e., the number of propagating Bloch states in the momentum space. For the [001] direction in $RuO_2$, the distribution of conduction channels for up-spin ($N_\parallel^\uparrow$) and down-spin ($N_\parallel^\downarrow$) electrons in the two-dimensional Brillouin zone (2DBZ) have congruent shapes (Fig. S2(b) [18]). $N_\parallel^\uparrow$ and $N_\parallel^\downarrow$ can be transformed to each other by a 90° rotation around the $\bar{\Gamma}$ point, reflecting the respective property of the $RuO_2$ Fermi surface [Fig. 2(c)]. At the same time, the distribution of conduction channels in $CrO_2$ (001) has fourfold rotational symmetry inherited from its Fermi surface [Fig. 2(d)]. As a result, an MTJ combining AFM $RuO_2$ and FM $CrO_2$ electrodes is not expected to produce TMR along the [001] direction, since the total transmission of the MTJ with opposite magnetization directions is to be the same.

In contrast, $RuO_2$ is spin polarized along the [110] direction. This is seen from the calculated distribution of conduction channels, $N_\parallel^\uparrow$ and $N_\parallel^\downarrow$, shown in Fig. 2(g), where a $RuO_2$ (110) supercell is used in the calculation [Fig. 2(e)]. For up-spin electrons [Fig. 2(g), left], there is an elliptic electron pocket elongated in the $\bar{\Gamma}$-$\bar{Y}$ direction (band 1) and overlapped with a rhombic hole pocket around the $\bar{\Gamma}$ point (band 2), and a small pocket at the $\bar{Y}$ point. Band 2 has two conduction channels on its own, resulting in $N_\parallel^\uparrow = 3$ in the regions of overlap with band 1. There is also a small hole pocket of $N_\parallel^\uparrow = 1$ at the $\bar{Z}$ point (band 2′). The same kind of Fermi-surface sheets, but rotated by 90° around the [001] axis, contribute to down-spin conduction channels of $RuO_2$ [Fig. 2(g), right]. Due to no overlap between their projections, $N_\parallel^\downarrow = 1$ in all regions of the 2DBZ where these bands appear. For $CrO_2$ (110), only up-spin Bloch states are present. As seen from Fig. 2(i), there is a large electron pocket around the 2DBZ center (band 1) with $N_\parallel^\uparrow = 1$ that alters to $N_\parallel^\uparrow = 2$ closer to the $\bar{Y}$ point. There is also a large hole pocket at the $\bar{Z}$ point (band 2). This distribution of conduction channels for $RuO_2$ (110) and $CrO_2$ (110) is consistent with the band-decomposed Fermi surfaces (Fig. S3 [18]).

The unbalanced distribution of $N_\parallel^\uparrow$ and $N_\parallel^\downarrow$ in $RuO_2$ (110) leads to $\vec{k}_\parallel$-dependent spin polarization $p_\parallel(\vec{k}_\parallel) = \frac{N_\parallel^\uparrow - N_\parallel^\downarrow}{N_\parallel^\uparrow + N_\parallel^\downarrow}$ and nonzero net-spin polarization $p = \frac{\sum N_\parallel^\uparrow - \sum N_\parallel^\downarrow}{\sum N_\parallel^\uparrow + \sum N_\parallel^\downarrow}$. As seen from Fig. 2(h), $p_\parallel = \pm 100\%$ in the regions of a finite $N_\parallel^{\uparrow,\downarrow}$ for one spin and zero $N_\parallel^{\uparrow,\downarrow}$ for another. Unlike $RuO_2$ (001), the net-spin polarization is nonvanishing for $RuO_2$ (110), namely $p = 31\%$, which is comparable to the spin polarization of representative FM metals like Fe, Co, and Ni [61,62]. Thus, $RuO_2$ (110) can be used as a spin detector in MTJs with a single FM electrode.

To demonstrate this behavior, we construct an MTJ using a FM $CrO_2$ electrode, an AFM $RuO_2$ counterelectrode, and a $TiO_2$ barrier layer. All constituents of this MTJ have the rutile structure and similar lattice constants [57,63,64], providing a possibility for epitaxial growth of the crystalline MTJ. We first consider a $RuO_2/TiO_2/CrO_2$ (110) MTJ with atomic structure shown in Fig. 3(a). As follows from the calculated density of states (DOS), the MTJ maintains a wide band gap of $TiO_2$ barrier with the Fermi energy $E_F$ located nearly in the middle [Fig. 3(b)]. We define parallel ($P$) and antiparallel ($AP$) states of the MTJ for the Cr moments parallel and antiparallel to the $Ru_A$ moments, respectively.

Figure 3(c) shows the calculated $\vec{k}_\parallel$-resolved transmission for the $P$ state of the MTJ, $T_P(\vec{k}_\parallel)$, and for the AP state, $T_{AP}(\vec{k}_\parallel)$. Due to $CrO_2$ being half metal, only up-spin electrons contribute to $T_P$ and down-spin electrons to $T_{AP}$. We find that $T_P(\vec{k}_\parallel)$ and $T_{AP}(\vec{k}_\parallel)$ mirror the distribution patterns of the $RuO_2$ (110) conduction channels, $N_\parallel^\uparrow$ and $N_\parallel^\downarrow$, respectively [compare Figs. 2(g) and 3(c)]. For up-spin electrons [Fig. 3(c), left], the largest contribution to $T_P(\vec{k}_\parallel)$ comes from band 1 at the Fermi surface, whereas other bands contribute modestly. In contrast, for down-spin electrons [Fig. 3(c), right], band 1 is elongated in the transport direction and its contribution to the transmission is small. The largest contribution to $T_{AP}(\vec{k}_\parallel)$ comes from band 2 that has a rounded-square shape with a hole around the $\bar{\Gamma}$ point. For both $T_P(\vec{k}_\parallel)$ and $T_{AP}(\vec{k}_\parallel)$, an area around the

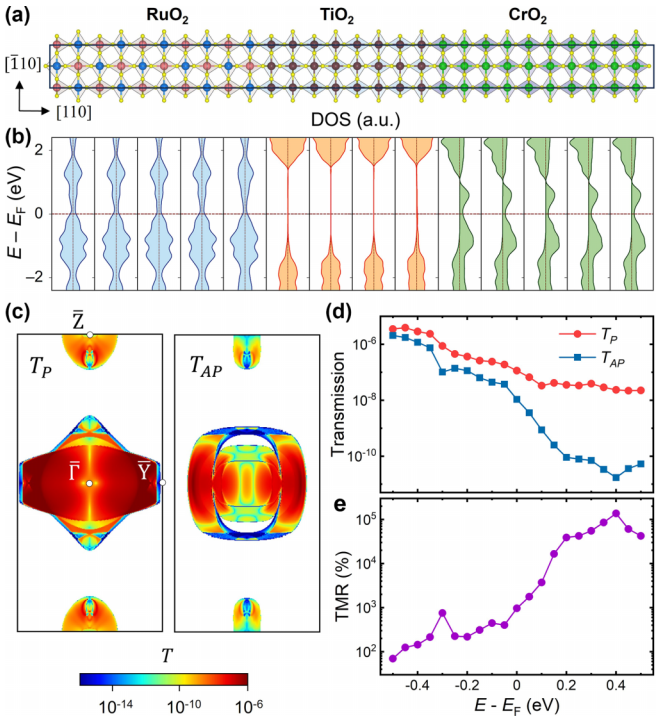


FIG. 3. (a) Atomic structure of $RuO_2/TiO_2/CrO_2$ (110) MTJ. (b) Calculated layer-resolved density of states (DOS) for the MTJ shown in (a). The horizontal line indicates the Fermi energy. (c) Calculated $\vec{k}_\parallel$-resolved transmission in the 2DBZ for *P*- (left) and *AP* (right) states of the MTJ. (d), (e) Calculated total transmissions, $T_P$ and $T_{AP}$, for *P* and *AP* states of the MTJ (d) and TMR (e) as functions of energy.

$\bar{\Gamma}$-$\bar{Y}$ line dominates in transmission, which is supported by the distribution of the decay rate $\kappa(\vec{k}_\parallel)$ of the two lowest-$\kappa$ evanescent states in the 2DBZ (Fig. S4(b) [18]). It is notable that $T_P(\vec{k}_\parallel)$ and $T_{AP}(\vec{k}_\parallel)$ have sizably reduced transmission at the $\bar{\Gamma}$ point and along the $\bar{\Gamma}$-$\bar{Z}$ line. This can be explained based on symmetry analysis [18].

By integrating over $\vec{k}_\parallel$, we find that total transmission $T_P$ is significantly greater than $T_{AP}$, leading to a giant TMR ratio $\frac{T_P - T_{AP}}{T_{AP}}$ of about 1000%. This value is comparable to the theoretically predicted value [10] and larger than the measured values [5,6] of TMR for the well-known Fe/MgO/Fe (001) MTJs. Figure 3(d) shows total transmissions, $T_P$ and $T_{AP}$, as functions of energy $E$ for the $RuO_2/TiO_2/CrO_2$ (110) MTJ. It is seen that both $T_P$ and $T_{AP}$ decrease with increasing $E$, $T_P$ being always greater than $T_{AP}$. This decrease originates from $\kappa(E)$ increasing with energy for the evanescent state with the lowest $\kappa$ near $E_F$ (Fig. S4(a) [18]). $T_{AP}$ as a function of energy decreases notably faster than $T_P$ due to the reduced contribution from the $RuO_2$ hole pocket [band 2 in Fig. 2(c)] that shrinks at higher energies. This leads to massive enhancement of TMR [Fig. 3(e)].

Contrary to $RuO_2$ (110), $RuO_2$ (001) supports only spin-neutral longitudinal currents. As a result (and as we have argued above), no TMR seems to appear in MTJs with $RuO_2$ (001) and FM electrodes, due to zero spin polarization of $RuO_2$ (001). However, rutile $MO_2$ ($M$ is a transition-metal element) is composed of chains of edge-sharing $MO_6$

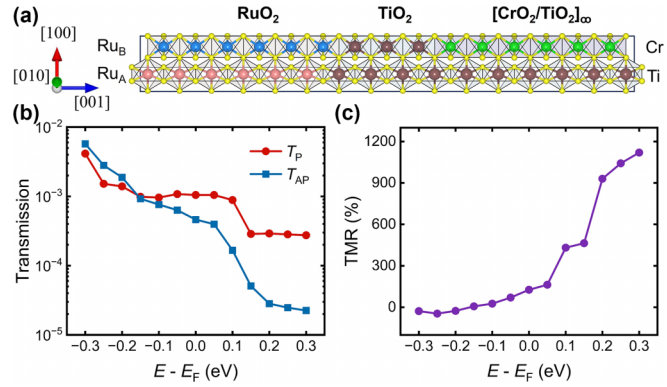


FIG. 4. (a) Atomic structure of $RuO_2/TiO_2/[CrO_2/TiO_2]_\infty$ (001) MTJ. (b), (c) Calculated transmission, $T_P$ and $T_{AP}$, for magnetic moments of Cr atoms parallel and antiparallel to $Ru_A$ atoms (b) and TMR (c) as functions of energy for the MTJ shown in (a).

octahedra along the [001] direction, where the adjacent chains share common corners of the octahedra [Fig. 4(a)]. This structural feature favors strong intrachain transport, and hence staggered spin currents in $RuO_2$ along the $Ru_A$ and $Ru_B$ chains [17]. Since such chains of octahedra are persistent across the interfaces in a perfectly epitaxial rutile heterostructure with the [001] growth direction [Fig. 4(a)], Néel spin currents are expected to dominate the spin-dependent transport properties of the rutile MTJ. This property allows engineering rutile MTJs that utilize $RuO_2$ (001) and FM electrodes and exhibit nonvanishing TMR.

To demonstrate this possibility, we consider a $RuO_2/TiO_2/[CrO_2/TiO_2]_n/CrO_2$ (001) MTJ, where $[CrO_2/TiO_2]_n$ represents a superlattice of alternating $TiO_2$ (001) and $CrO_2$ (001) monolayers with $n$ repeats. Such a superlattice can be fabricated using modern thin-film growth techniques [65,66]. Layer-by-layer deposition of the superlattice provides alternating growth of the $TiO_6$ and $CrO_6$ chains. This leads to different effective barrier thickness for the Néel spin currents flowing on the $Ru_A$ and $Ru_B$ sublattices, generating TMR [Fig. 1(b)]. For simplicity, we assume a $RuO_2/TiO_2/[CrO_2/TiO_2]_\infty$ (001) MTJ, where the right electrode is an infinite $CrO_2/TiO_2$ superlattice ($n = \infty$) [Fig. 4(a)]. We find that $CrO_6$ chains behave as a half metal while $TiO_6$ chains as an insulator (Figs. S5(b) and S5(c) [18]), indicating that this MTJ can be considered as an extreme case of an MTJ with different effective barrier thickness for two magnetic sublattices.

For an MTJ with 7-monolayer-thick $TiO_2$, $T_P$ appears to be more than a factor of 2 higher than $T_{AP}$, resulting in a sizable TMR ratio of 127%. Changing electron energy $E$ alters $T_P$ and $T_{AP}$ [Fig. 4(b)], as well as TMR [Fig. 4(c)], reflecting changes in the effective transport spin polarization of the Néel spin current in $RuO_2$ (Fig. S10(d) [18]). The TMR ratio varies from small negative values at $E = E_F - 0.3$ eV to very large positive values exceeding 1000% at $E = E_F + 0.3$ eV, due to the enhanced spin polarization at higher energies. We note that the predicted TMR for $RuO_2/TiO_2/[CrO_2/TiO_2]_n$ (001) MTJs oscillates as a function of $TiO_2$ thickness [18], which can be verified experimentally. Also, a sizable TMR appears in $RuO_2/TiO_2/[CrO_2/TiO_2]_n/CrO_2$ (001) MTJs with small

*n* [18], which can be conveniently realized by the delta-doping technique at the interface [65].

## III. CONCLUSIONS

Both proposed approaches to realize TMR in an MTJ with a single FM electrode are feasible in practice. The first approach utilizing $RuO_2$ (110) is more straightforward and can be employed in MTJs with barriers and FM electrodes different from $TiO_2$ and $CrO_2$. Compared to AFMTJs based on $RuO_2$ [17], it offers a simple practical test for using $RuO_2$ in functional spintronic devices due to simplicity of FM switching by an applied magnetic field. The second approach utilizing $RuO_2$ (001) requires a stringent control of the epitaxial layer-by-layer growth of the MTJ structure [65,66]. Realizing this approach experimentally would provide direct evidence of the Néel spin currents and demonstrate promising sublattice-resolved physics, such as spin torque on a single magnetic sublattice [67]. It also has advantage of the perpendicular-to-plane magnetic anisotropy of $RuO_2$ (001) [55] desirable for high-density memory applications. In addition, this approach can be realized in 2D lateral MTJs with a bilayer *A*-type AFM electrode and a bilayer FM electrode, where the effective barrier width can be controlled independently for each layer by the recently developed edge-epitaxy technique [68–70]. We hope, therefore, that our theoretical predictions will stimulate experimental studies of the proposed MTJs and development of associated spintronic devices.

*Note added.* While finalizing our manuscript, we became aware of the recently published paper [71].

## ACKNOWLEDGMENTS

This work was primarily supported by the Division of Materials Research of the National Science Foundation (NSF Grant No. DMR-2316665). Research at HFIPS was supported by the National Natural Science Foundation of China (Grants No. 12274411, No. 12241405, and No. 52250418), the Basic Research Program of the Chinese Academy of Sciences (CAS) Based on Major Scientific Infrastructures (Grant No. JZHKYPT-2021–08), and the CAS Project for Young Scientists in Basic Research Grant No. YSBR-084. Research at the South Dakota School of Mines and Technology was supported by the South Dakota Board of Regents Competitive Research Grant No. 2021. Computations were performed at the University of Nebraska-Lincoln Holand Computing Center and Hefei Advanced Computing Center.

[1] *Spintronics Handbook: Spin Transport and Magnetism*, 2nd ed., edited by E. Y. Tsymbal, and I. Žutić (CRC Press, Boca Raton, 2019).

[2] M. Julliere, Tunneling between ferromagnetic films, Phys. Lett. A **54**, 225 (1975).

[3] R. Meservey and P. M. Tedrow, Spin-polarized electron tunneling, Phys. Rep. **238**, 173 (1994).

[4] J. S. Moodera, L. R. Kinder, T. M. Wong, and R. Meservey, Large magnetoresistance at room temperature in ferromagnetic thin film tunnel junctions, Phys. Rev. Lett. **74**, 3273 (1995).

[5] S. Yuasa, T. Nagahama, A. Fukushima, Y. Suzuki, and K. Ando, Giant room-temperature magnetoresistance in single-crystal Fe/MgO/Fe magnetic tunnel junctions, Nat. Mater. **3**, 868 (2004).

[6] S. Parkin, C. Kaiser, A. Panchula, P. M. Rice, B. Hughes, M. Samant, and S. H. Yang, Giant tunnelling magnetoresistance at room temperature with MgO (100) tunnel barriers, Nat. Mater. **3**, 862 (2004).

[7] E. Y. Tsymbal, O. N. Mryasov, and P. R. LeClair, Spin-dependent tunneling in magnetic tunnel junctions, J. Phys.: Condens. Matter **15**, R109 (2003).

[8] *Introduction to Magnetic Random-Access Memory*, edited by B. Dieny, R. B. Goldfarb, and K.-J. Lee (Wiley-IEEE Press, 2016).

[9] Ph. Mavropoulos, N. Papanikolaou, and P. H. Dederichs, Complex band structure and tunneling through ferromagnet/insulator/ferromagnet junctions, Phys. Rev. Lett. **85**, 1088 (2000).

[10] W. H. Butler, X.-G. Zhang, T. C. Schulthess, and J. M. MacLaren, Spin-dependent tunneling conductance of Fe|MgO|Fe sandwiches, Phys. Rev. B **63**, 054416 (2001).

[11] J. Velev, K. D. Belashchenko, D. A. Stewart, M. van Schilfgaarde, S. S. Jaswal, and E. Y. Tsymbal, Negative spin polarization and large tunneling magnetoresistance in epitaxial Co|$SrTiO_3$|Co magnetic tunnel junctions, Phys. Rev. Lett. **95**, 216601 (2005).

[12] J. M. De Teresa, A. Barthélémy, A. Fert, J. P. Contour, F. Montaigne, and P. Seneor, Role of metal-oxide interface in determining the spin polarization of magnetic tunnel junctions, Science **286**, 507 (1999).

[13] A. Fert, Nobel Lecture: Origin, development, and future of spintronics, Rev. Mod. Phys. **80**, 1517 (2008).

[14] K. D. Belashchenko, E. Y. Tsymbal, M. van Schilfgaarde, D. Stewart, I. I. Oleinik, and S. S. Jaswal, Effect of interface bonding on spin-dependent tunneling from the oxidized Co surface, Phys. Rev. B **69**, 174408 (2004).

[15] I. Adagideli, G. E. W. Bauer, and B. I. Halperin, Detection of current-induced spins by ferromagnetic contacts, Phys. Rev. Lett. **97**, 256601 (2006).

[16] K. Samanta, D.-F. Shao, T. R. Paudel, and E. Y. Tsymbal, Giant tunneling magnetoresistance in magnetic tunnel junctions with a single ferromagnetic electrode, Abstracts of the 68th Annual MMM Conference (Dallas, TX, 2023).

[17] D.-F. Shao, Y.-Y. Jiang, J. Ding, S.-H. Zhang, Z.-A. Wang, R.-C. Xiao, G. Gurung, W. J. Lu, Y. P. Sun, and E. Y. Tsymbal, Néel spin currents in antiferromagnets, Phys. Rev. Lett. **130**, 216702 (2023).

[18] See Supplemental Material at http://link.aps.org/supplemental/10.1103/PhysRevB.109.174407 for details of theoretical calculations, electronic structure of bulk $RuO_2$ and $CrO_2$, projected and bulk band-decomposed Fermi surfaces of $RuO_2$ and $CrO_2$, symmetry analysis of transmission in a $RuO_2/TiO_2/CrO_2$ (110) MTJ, density of states of a $[TiO_2/CrO_2]_\infty$ (001) superlattice, complex band structure of $TiO_2$ (001), distribution of conduction channels in $[CrO_2/TiO_2]_\infty$ (001) and $RuO_2$

(001), momentum-dependent transmission and oscillatory TMR in a $RuO_2/TiO_2/[TiO_2/CrO_2]_\infty$ (001) MTJ which includes Refs. [19–35].

[19] P. Hohenberg and W. Kohn, Inhomogeneous electron gas, Phys. Rev. **136**, B864 (1964).

[20] G. Kresse and J. Furthmuller, Efficient iterative schemes for ab initio total-energy calculations using a plane-wave basis set, Phys. Rev. B **54**, 11169 (1996).

[21] G. Kresse and D. Joubert, From ultrasoft pseudopotentials to the projector augmented-wave method, Phys. Rev. B **59**, 1758 (1999).

[22] P. E. Blöchl, Projector augmented-wave method, Phys. Rev. B **50**, 17953 (1994).

[23] J. P. Perdew, K. Burke, and M. Ernzerhof, Generalized gradient approximation made simple, Phys. Rev. Lett. **77**, 3865 (1996).

[24] V. V. Anisimov, J. Zaanen, and O. K. Andersen, Band theory and Mott insulators: Hubbard *U* instead of Stoner *I*, Phys. Rev. B **44**, 943 (1991).

[25] S. L. Dudarev, G. A. Botton, S. Y. Savrasov, C. J. Humphreys, and A. P. Sutton, Electron-energy-loss spectra and the structural stability of nickel oxide: An LSDA+U study, Phys. Rev. B **57**, 1505 (1998).

[26] N. Marzari, A. A. Mostofi, J. R. Yates, I. Souza, and D. Vanderbilt, Maximally localized Wannier functions: Theory and applications, Rev. Mod. Phys. **84**, 1419 (2012).

[27] I. Souza, N. Marzari, and D. Vanderbilt, Maximally localized Wannier functions for entangled energy bands, Phys. Rev. B **65**, 035109 (2001).

[28] G. Pizzi, V. Vitale, R. Arita, S. Blügel, F. Freimuth, G. Géranton, M. Gibertini, D. Gresch, C. Johnson, T. Koretsune, J. Ibañez-Azpiroz, H. Lee, J.-M. Lihm, D. Marchand, A. Marrazzo, Y. Mokrousov, J. I. Mustafa, Y. Nohara, Y. Nomura, L. Paulatto, S. Poncé, T. Ponweiser, J. Qiao, F. Thöle, S. S. Tsirkin, M. Wierzbowska, N. Marzari, D. Vanderbilt, I. Souza, A. A. Mostofi, and J. R. Yates, Wannier90 as a community code: new features and applications, J. Phys.: Condens. Matter **32**, 165902 (2020).

[29] A. Kokalj, XCrySDen − a new program for displaying crystalline structures and electron densities, J. Mol. Graph. Model. **17**, 176 (1999).

[30] J. Taylor, H. Guo, and J. Wang, Ab initio modeling of quantum transport properties of molecular electronic devices, Phys. Rev. B **63**, 245407 (2001).

[31] M. Brandbyge, J.-L. Mozos, P. Ordejón, J. Taylor, and K. Stokbro, Density-functional method for nonequilibrium electron transport, Phys. Rev. B **65**, 165401 (2002).

[32] S. Smidstrup, T. Markussen, P. Vancraeyveld, J. Wellendorff, J. Schneider, T. Gunst, B. Verstichel, D. Stradi, P. A. Khomyakov, U. G. Vej-Hansen, M.-E. Lee, S. T. Chill, F. Rasmussen, G. Penazzi, F. Corsetti, A. Ojanperä, K. Jensen, L. N. Palsgaard Mattias, U. Martinez, A. Blom, M. Brandbyge, and K. Stokbro, QuantumATK: an integrated platform of electronic and atomic-scale modelling tools, J. Phys.: Condens. Matter **32**, 015901 (2020); QuantumATK, version P-2016.3, https://www.synopsys.com/manufacturing/quantumatk.html.

[33] K. Momma and F. Izumi, *VESTA3* for three-dimensional visualization of crystal, volumetric and morphology data, J. Appl. Crystallogr. **44**, 1272 (2011).

[34] T. Williams and C. Kelley, Gnuplot 5.2: An interactive plotting program, http://gnuplot.info/docs_5.2/Gnuplot_5.2.pdf (2017).

[35] J. D. Hunter, Matplotlib: A 2D graphics environment, Comput. Sci. Eng. **9**, 90 (2007).

[36] S. Hayami, Y. Yanagi, and H. Kusunose, Momentum-dependent spin splitting by collinear antiferromagnetic ordering, J. Phys. Soc. Jpn. **88**, 123702 (2019).

[37] L.-D. Yuan, Z. Wang, J.-W. Luo, E. I. Rashba, and A. Zunger, Giant momentum-dependent spin splitting in centrosymmetric low-Z antiferromagnets, Phys. Rev. B **102**, 014422 (2020).

[38] L.-D. Yuan, Z. Wang, J.-W. Luo, and A. Zunger, Prediction of low-Z collinear and noncollinear antiferromagnetic compounds having momentum-dependent spin splitting even without spin-orbit coupling, Phys. Rev. Mater. **5**, 014409 (2021).

[39] M. Naka, S. Hayami, H. Kusunose, Y. Yanagi, Y. Motome, and H. Seo, Spin current generation in organic antiferromagnets, Nat. Commun. **10**, 4305 (2019).

[40] R. González-Hernández, L. Šmejkal, K. Výborný, Y. Yahagi, J. Sinova, T. Jungwirth, and J. Železný, Efficient electrical spin-splitter based on non-relativistic collinear antiferromagnetism, Phys. Rev. Lett. **126**, 127701 (2021).

[41] H. Y. Ma, M. Hu, N. Li, J. Liu, W. Yao, J.-F. Jia, and J. Liu, Multifunctional antiferromagnetic materials with giant piezomagnetism and noncollinear spin current, Nat. Commun. **12**, 2846 (2021).

[42] L. Šmejkal, J. Sinova, and T. Jungwirth, Beyond conventional ferromagnetism and antiferromagnetism: A phase with nonrelativistic spin and crystal rotation symmetry, Phys. Rev. X **12**, 031042 (2022).

[43] L. Šmejkal, J. Sinova, and T. Jungwirth, Emerging research landscape of altermagnetism, Phys. Rev. X **12**, 040501 (2022).

[44] I. Mazin, Editorial: Altermagnetism—A new punch line of fundamental magnetism, Phys. Rev. X **12**, 040002 (2022).

[45] J. Železný, Y. Zhang, C. Felser, and B. Yan, Spin-polarized current in noncollinear antiferromagnets, Phys. Rev. Lett. **119**, 187204 (2017).

[46] G. Gurung, D.-F. Shao, and E. Y. Tsymbal, Transport spin polarization of noncollinear antiferromagnetic antiperovskites, Phys. Rev. Mater. **5**, 124411 (2021).

[47] D.-F. Shao, S.-H. Zhang, M. Li, C. B. Eom, and E. Y. Tsymbal, Spin-neutral currents for spintronics, Nat. Commun. **12**, 7061 (2021).

[48] J. Dong, X. Li, G. Gurung, M. Zhu, P. Zhang, F. Zheng, E. Y. Tsymbal, and J. Zhang, Tunneling magnetoresistance in noncollinear antiferromagnetic tunnel junctions, Phys. Rev. Lett. **128**, 197201 (2022).

[49] L. Šmejkal, A. Birk Hellenes, R. González-Hernández, J. Sinova, and T. Jungwirth, Giant and tunneling magnetoresistance in unconventional collinear antiferromagnets with nonrelativistic spin-momentum coupling, Phys. Rev. X **12**, 011028 (2022).

[50] P. Qin, H. Yan, X. Wang, H. Chen, Z. Meng, J. Dong, M. Zhu, J. Cai, Z. Feng, X. Zhou, L. Liu, T. Zhang, Z. Zeng, J. Zhang, C. Jiang, and Z. Liu, Room-temperature magnetoresistance in an all-antiferromagnetic tunnel junction, Nature (London) **613**, 485 (2023).

[51] X. Chen, T. Higo, K. Tanaka, T. Nomoto, H. Tsai, H. Idzuchi, M. Shiga, S. Sakamoto, R. Ando, H. Kosaki, T. Matsuo, D. Nishio-Hamane, R. Arita, S. Miwa, and S. Nakatsuji, Octupole-driven magnetoresistance in an antiferromagnetic tunnel junction, Nature (London) **613**, 490 (2023).

[52] G. Gurung, D.-F. Shao, and E. Y. Tsymbal, Extraordinary tunneling magnetoresistance in antiferromagnetic tunnel junctions with antiperovskite electrodes, arXiv:2306.03026 [cond-mat.mtrl-sci].

[53] Y.-Y. Jiang, Z.-A. Wang, K. Samanta, S.-H. Zhang, R.-C. Xiao, W. J. Lu, Y. P. Sun, E. Y. Tsymbal, and D.-F. Shao, Prediction of giant tunneling magnetoresistance in $RuO_2/TiO_2/RuO_2$ (110) antiferromagnetic tunnel junctions, Phys. Rev. B **108**, 174439 (2023).

[54] H. Bai, Y. C. Zhang, L. Han, Y. J. Zhou, F. Pan, and C. Song, Antiferromagnetism: An efficient and controllable spin source, Appl. Phys. Rev. **9**, 041316 (2022).

[55] T. Berlijn, P. C. Snijders, O. Delaire H.-D. Zhou, T. A. Maier, H.-B. Cao, S.-X. Chi, M. Matsuda, Y. Wang, M. R. Koehler, P. R. C. Kent, and H. H. Weitering, Itinerant antiferromagnetism in $RuO_2$, Phys. Rev. Lett. **118**, 077201 (2017).

[56] K.-H. Ahn, A. Hariki, K.-W. Lee, and J. Kuneš, $RuO_2$ antiferromagnetism in as $d$-wave Pomeranchuk instability, Phys. Rev. B **99**, 184432 (2019).

[57] P. Porta, M. Marezio, J. P. Remeika, and P. D. Dernier, Chromium dioxide: High pressure synthesis and bond lengths, Mater. Res. Bull. **7**, 157 (1972).

[58] R. A. de Groot, F. M. Mueller, P. G. van Engen, and K. H. J. Buschow, New class of materials: Half-metallic ferromagnets, Phys. Rev. Lett. **50**, 2024 (1983).

[59] Y. Ji, G. J. Strijkers, F. Y. Yang, C. L. Chien, J. M. Byers, A. Anguelouch, G. Xiao, and A. Gupta, Determination of the spin polarization of half-metallic $CrO_2$ by point contact Andreev reflection, Phys. Rev. Lett. **86**, 5585 (2001).

[60] F. Bisti, V. A. Rogalev, M. Karolak, S. Paul, A. Gupta, T. Schmitt, G. Güntherodt, V. Eyert, G. Sangiovanni, G. Profeta, and V. N. Strocov, Weakly-correlated nature of ferromagnetism in nonsymmorphic $CrO_2$ revealed by bulk-sensitive soft-X-ray ARPES, Phys. Rev. X **7**, 041067 (2017).

[61] R. J. Soulen Jr., J. M. Byers, M. S. Osofsky, B. Nadgorny, T. Ambrose, S. F. Cheng, P. R. Broussard, C. T. Tanaka, J. Nowak, J. S. Moodera, A. Barry, and J. M. D. Coey, Measuring the spin polarization of a metal with a superconducting point contact, Science **282**, 85 (1998).

[62] S. K. Upadhyay, A. Palanisami, R. N. Louie, and R. A. Buhrman, Probing ferromagnets with Andreev reflection, Phys. Rev. Lett. **81**, 3247 (1998).

[63] C.-E. Boman, Refinement of the crystal structure of ruthenium dioxide, Acta Chem. Scand. **24**, 116 (1970).

[64] W. H. Baur and A. A. Khan, Rutile-type compounds. IV. $SiO_2$, $GeO_2$ and a comparison with other rutile-type structures, Acta Crystallogr. B **27**, 2133 (1971).

[65] R. Ramesh and D. G. Schlom, Creating emergent phenomena in oxide superlattices, Nat. Rev. Mater. **4**, 257 (2019).

[66] R. C. Haislmaier, G. Stone, N. Alem, and R. Engel-Herbert, Creating Ruddlesden-Popper phases by hybrid molecular beam epitaxy, Appl. Phys. Lett. **109**, 043102 (2016).

[67] S.-S. Zhang, Z.-A. Wang, B. Li, S.-H. Zhang, R.-C. Xiao, L.-X. Liu, X. Luo, W. J. Lu, M. Tian, Y. P. Sun, E. Y. Tsymbal, H. Du, and D.-F. Shao, X-Type antiferromagnets, arXiv:2310.13271.

[68] M.-Y. Li, Y. Shi, C.-C. Cheng, L.-S. Lu, Y.-C. Lin, H. Tang, M. Tsai, C. Chu, K. Wei, J.-H. He, W.-H. Chang, K. Suenaga, and L.-J. Li, Epitaxial growth of a monolayer $WSe_2$-$MoS_2$ lateral $p$-$n$ junction with an atomically sharp interface, Science **349**, 524 (2015).

[69] P. K. Sahoo, S. Memaran, Y. Xin, L. Balicas, and H. R. Gutiérrez, One-pot growth of two-dimensional lateral heterostructures via sequential edge-epitaxy, Nature (London) **553**, 63 (2018).

[70] Z. Zhang, P. Chen, X. Duan, K. Zang, J. Luo, and X. Duan, Robust epitaxial growth of two-dimensional heterostructures, multi-heterostructures, and superlattices, Science **357**, 788 (2017).

[71] B. Chi, L. Jiang, Y. Zhu, G. Yu, C. Wan, J. Zhang, and X. Han, Crystal-facet-oriented altermagnets for detecting ferromagnetic and antiferromagnetic states by giant tunneling magnetoresistance, Phys. Rev. Appl. **21**, 034038 (2024).